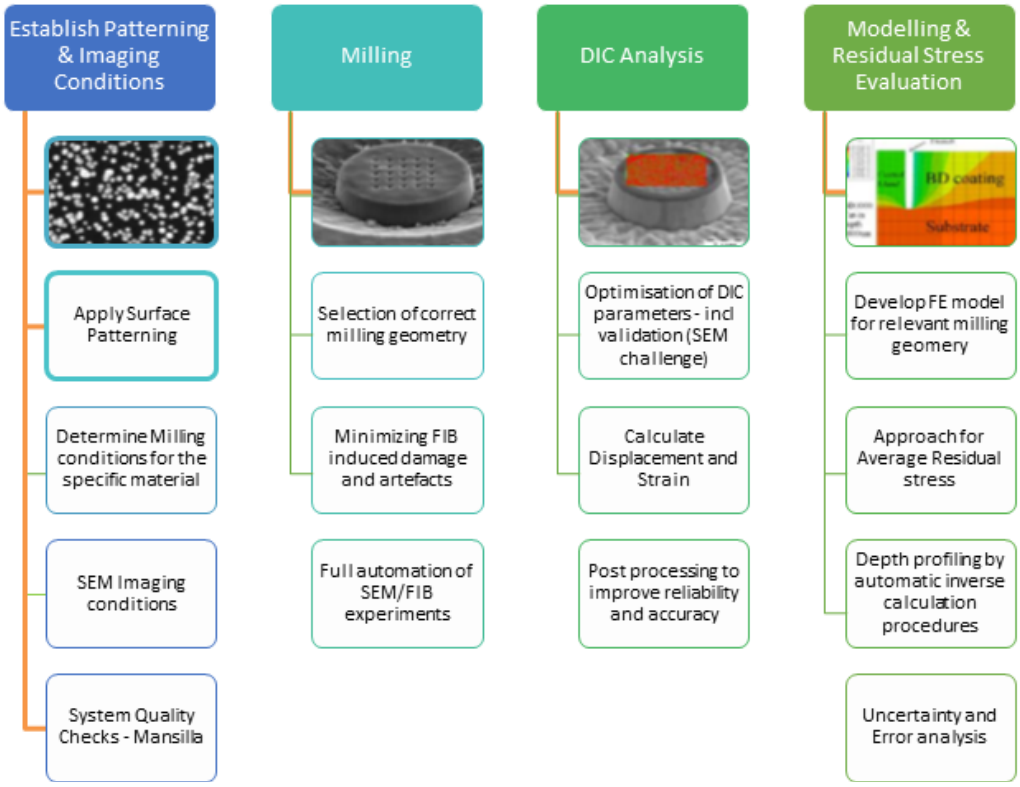

Fig. 1: Schematic description of ALL the experimental issues that were faced during the project in order to promote standardisation of the method

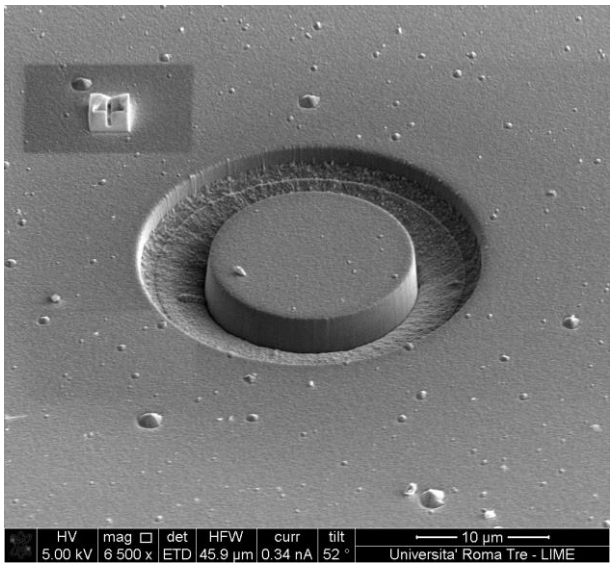

Fig.2: An example of FIB-DIC ring-core analysis on the produced reference TiN sample

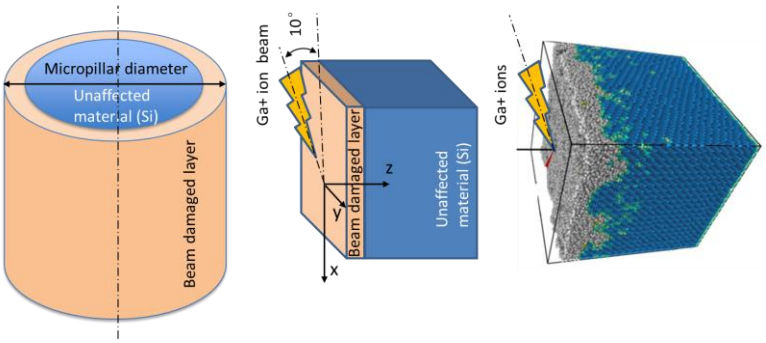

Fig. 3 Multi-scale modelling to understand the effect of ion-irradiation on strain relief after FIB annular milling.

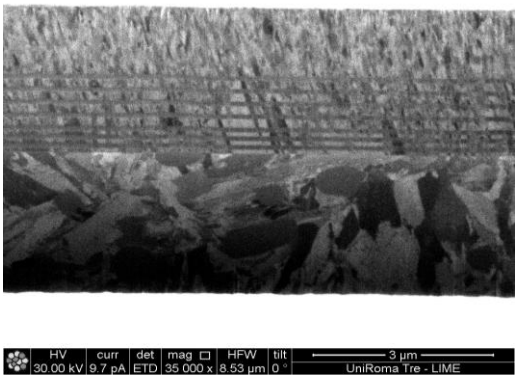

Fig. 4: The optimized multilayer coating for diesel injection systems developed at Bosch

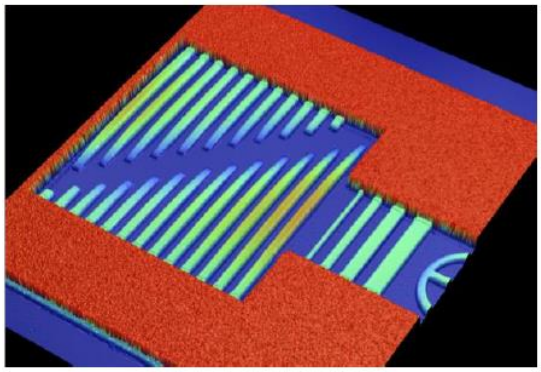

Fig. 5: The MEMS testing area on the new ISTRESS RF-switches Mask produced by Thales

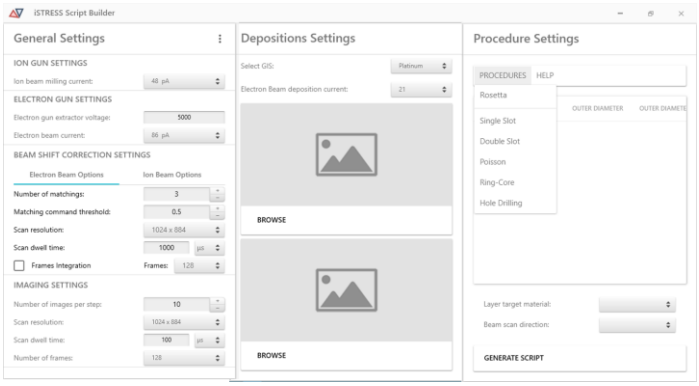

Fig. 6: GUI for semi-automatic FIB-DIC method developed at Roma Tre

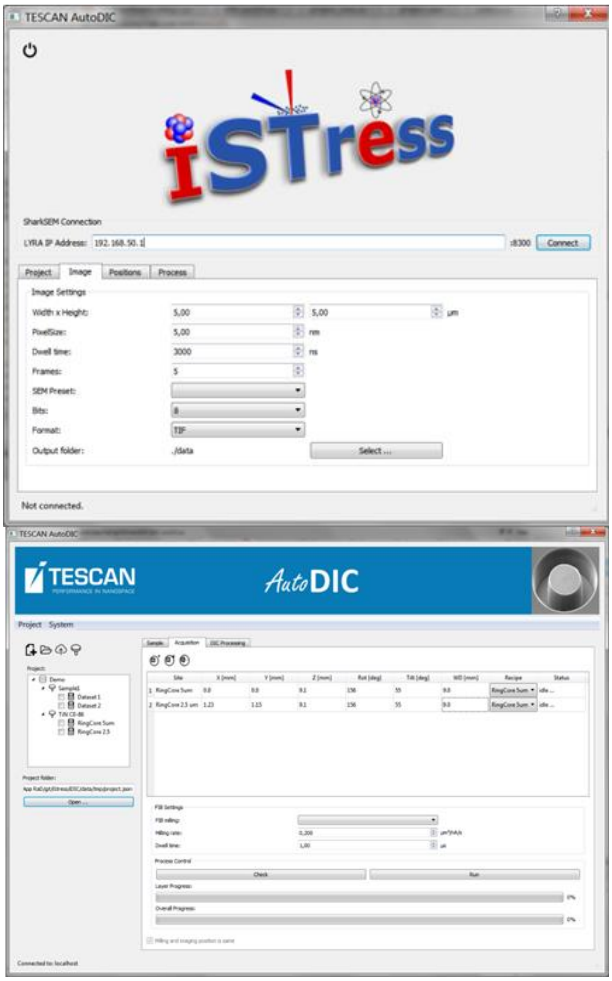

Fig. 7: Evolution of the graphical interface top: proof of concept tool, bottom: current software tool at the end of the project

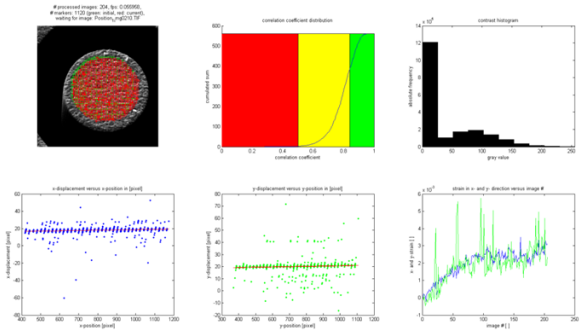

Fig. 8: An example of Run-Time DIC processing

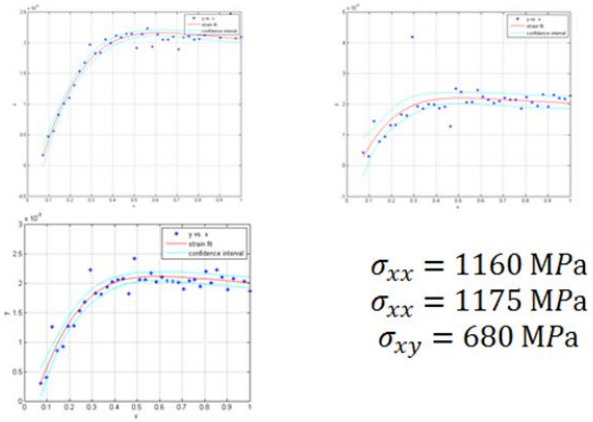

Fig. 9:Strain fitting and stress calculation

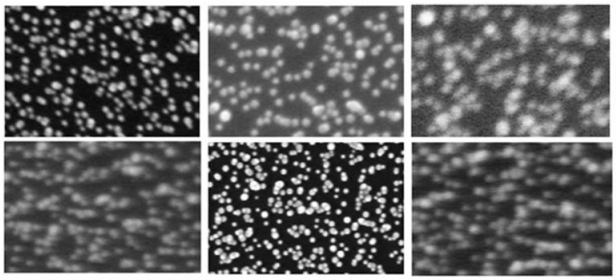

Fig. 10: Reference images of Pt dot patterns on Si from different ISTRESS partners

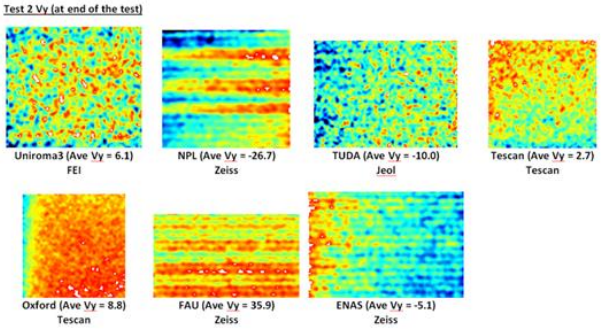

Fig. 11: A measure of stability of different Fib instruments

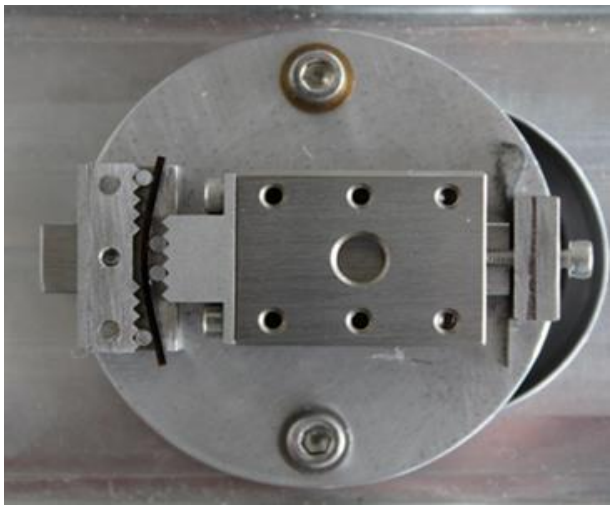

Fig. 12: in-situ bending device designed by TUDA

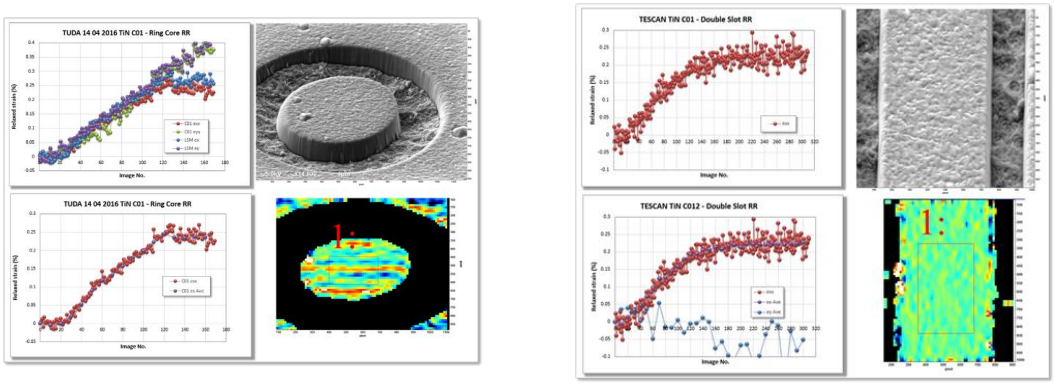

Fig. 13: Strain relief profile: Ring Core (left) and Double Slot (right)

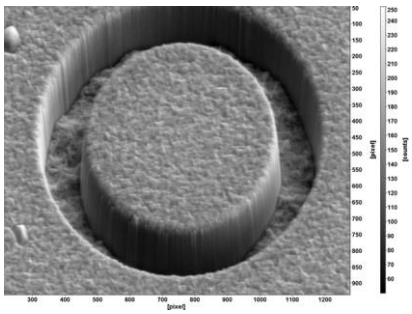

Fig. 14: Image Set 1: ETHZ 18 08 2015 TiN Ring Core
Good quality images, very stable
FEI Instrument

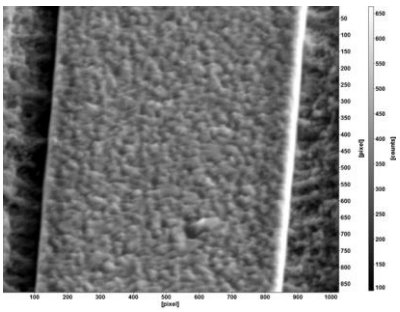

Fig. 15: Image set 2: Uniroma 03 09 2015 TiN Double Slot No tilt correction, Quite Noisy
FEI Instrument

Fig. 16: Representative data or strain relief for ring core geometry: Full set (left) and Average set (right)

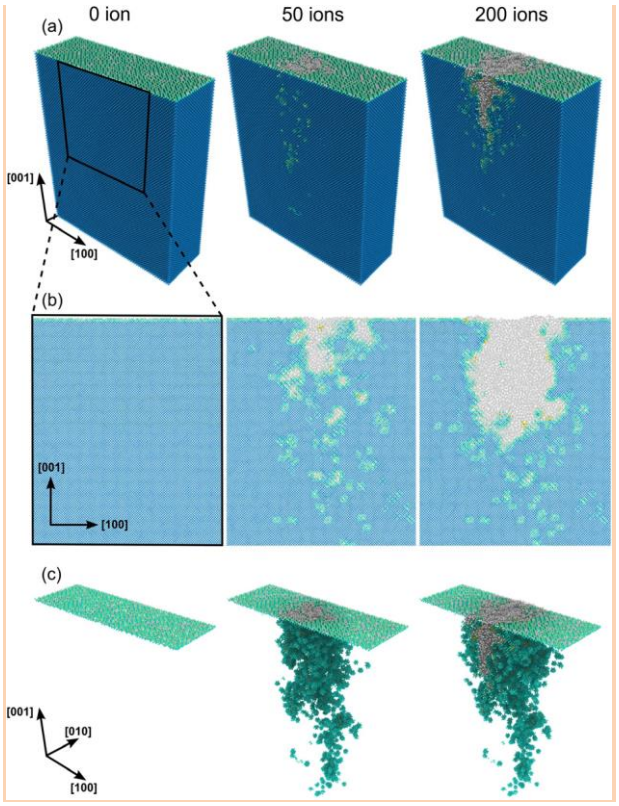

Induced damage in collision cascade simulations of 5 keV Ga+ ions in Si at 300 K

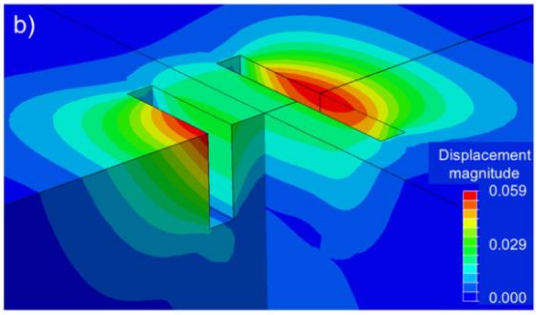

Finite element (FE) model of the H-bar showing the displacement magnitude.

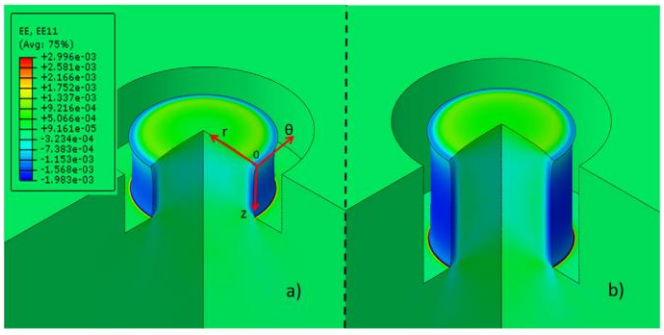

Example of radial residual elastic strain due to FIB ring-core milling imposing an eigenstrain profile.

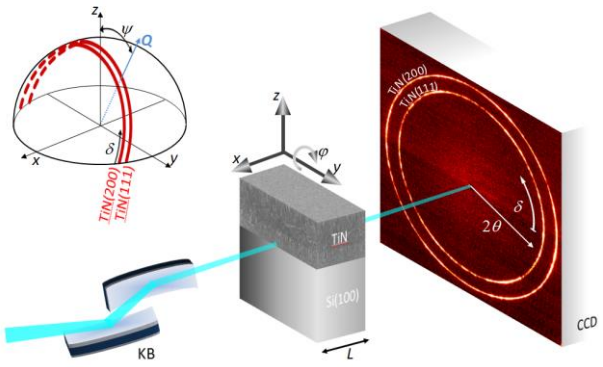

Fig. 17: A schematic view of the position-resolved X-ray nano-diffraction experiment carried out in transmission diffraction geometry

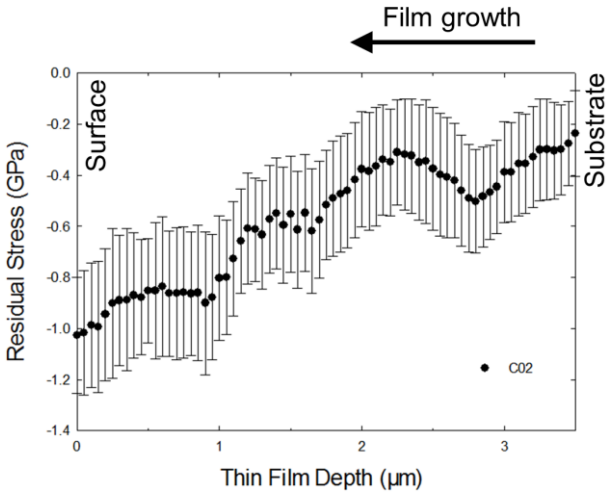

Fig. 18: In-plane stress profile in the reference TiN sample C02 as a function of the film thickness

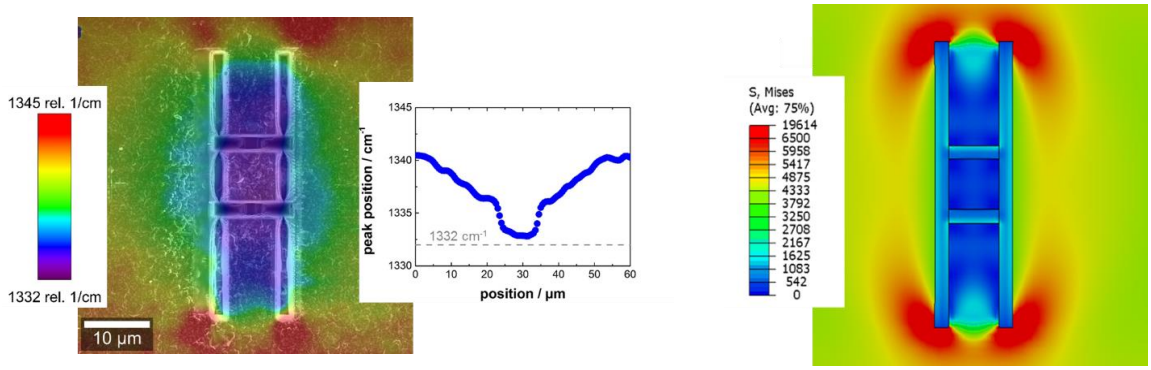

Fig. 19: (left) µ-Raman mapping of the four slot geometry together with Raman peak position across the four slot geometry and (right) Von Mises stress distribution obtained by FEA

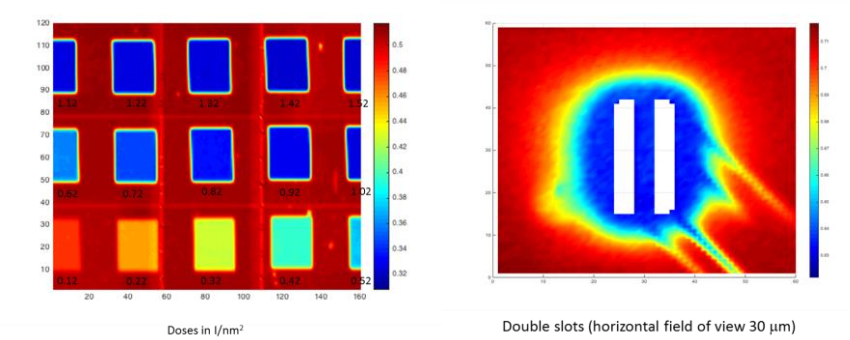

Fig. 20: (left) Amorphisation degree at several FIB doses (EBSD), (right) amorphisation at FIB-DIC geometry

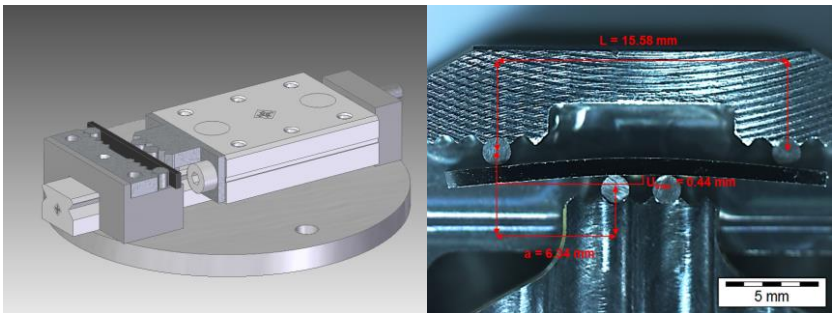

Fig. 21: Design and usage of the in-situ SEM four-point bending device

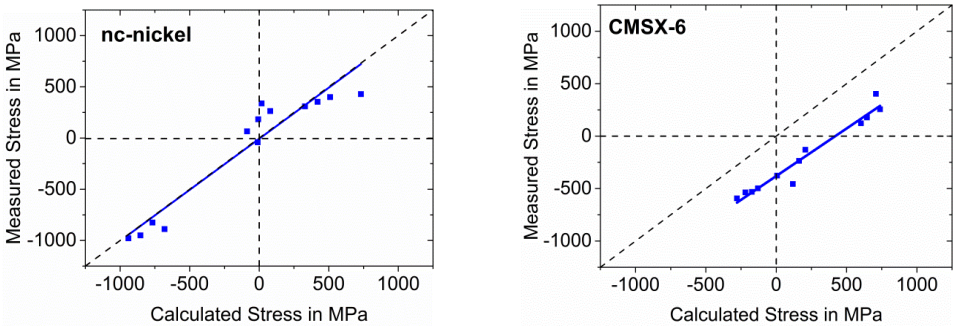

Fig. 22: Results of the measured and calculated bending gradient on nc-nickel and CMSX-6 sample

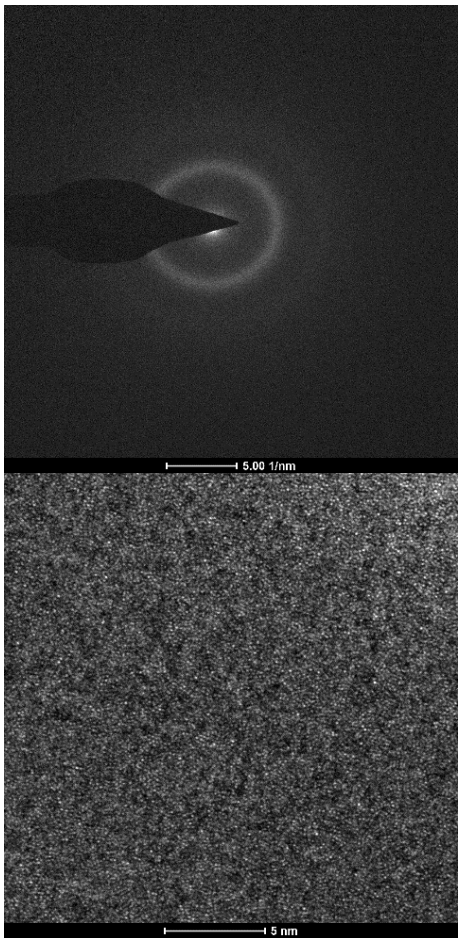

Fig. 23: TEM diffraction pattern and micrograph showing that the BMG is not fully amorphous but rather nano-crystalline

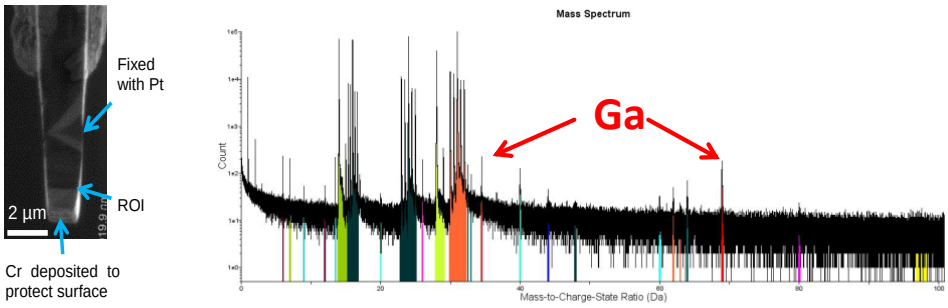

Fig. 24: (left) TiN sample mounted to a TEM grid; (right) Mass spectrum of TiN sample incl. the Ga peaks

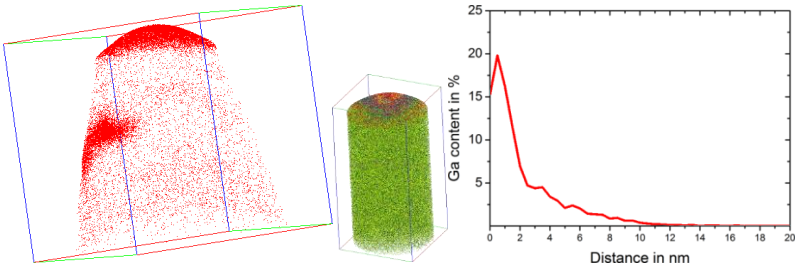

Fig. 25: (left) Ga atoms shown in red. Highest concentration close to top surface and at one side, (middle + right) Ga content in a cylinder from surface to middle region

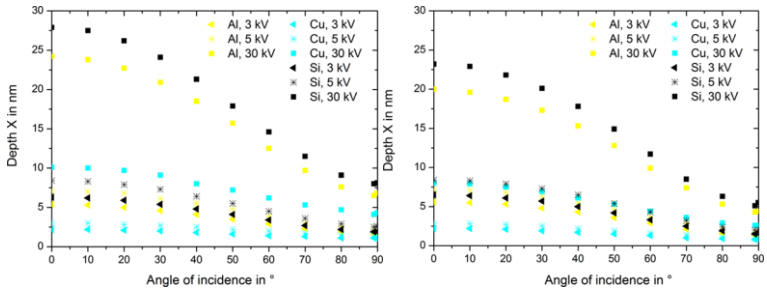

Fig. 26: (left) Ga, (right) Xe: Implantation depth of ions in Al, Cu and Si at 3 kV, 5 kV and 30 kV at different incident angles

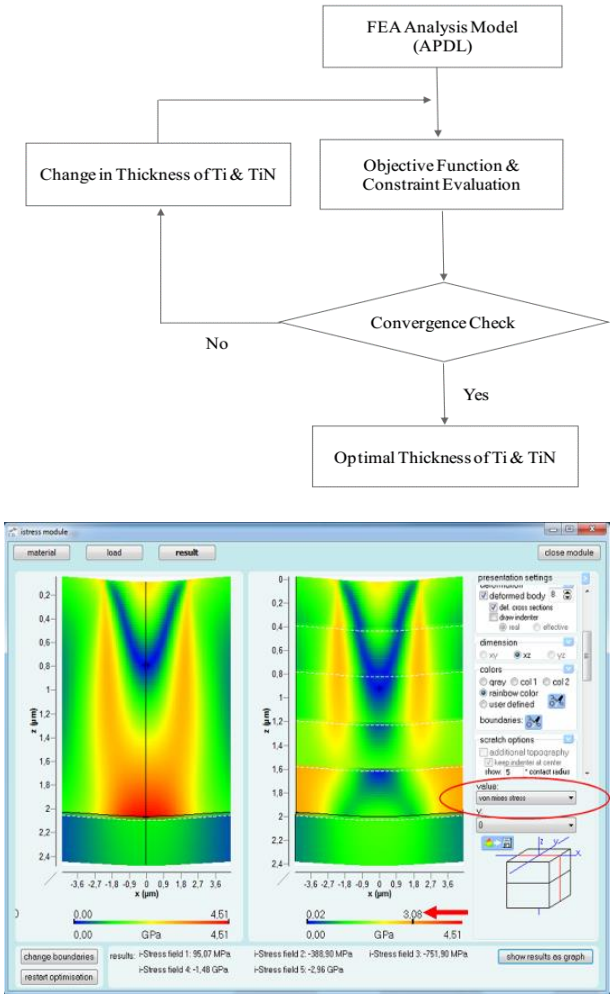

Fig. 27:Optimization frame work for FEM (top) and intrinsic stress optimization tool in FilmDoctor (bottom)

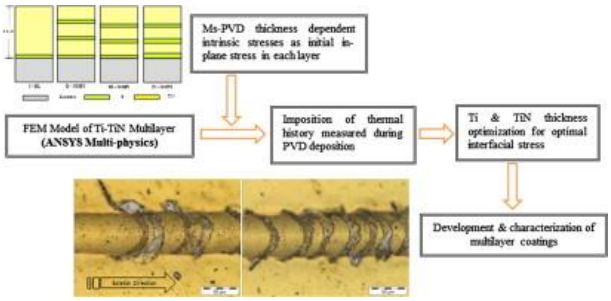

Fig. 28: Ti-TiN multilayer system designed with the ANSYS routine

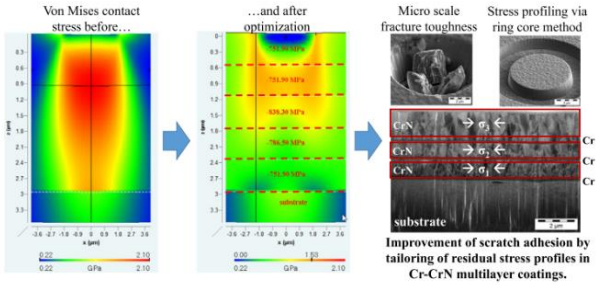

Fig. 29: Cr-CrN system designed with the intrinsic stress optimization tool within FilmDoctor

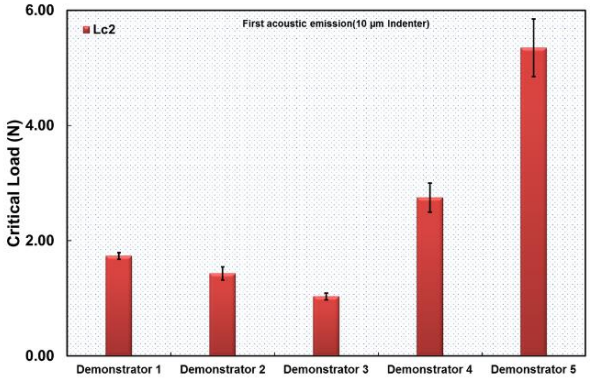

Fig. 30: Adhesion results of different demonstrators using 10 µm indenter

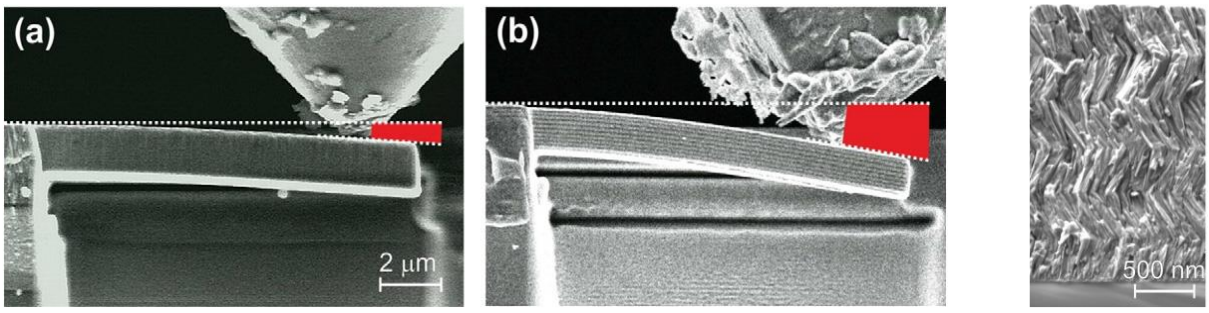

Fig. 31: Micro cantilever bending tests to evaluate the fracture toughness of different multilayer samples (left) and Interface geometry design using tilted brittle interfaces (right)

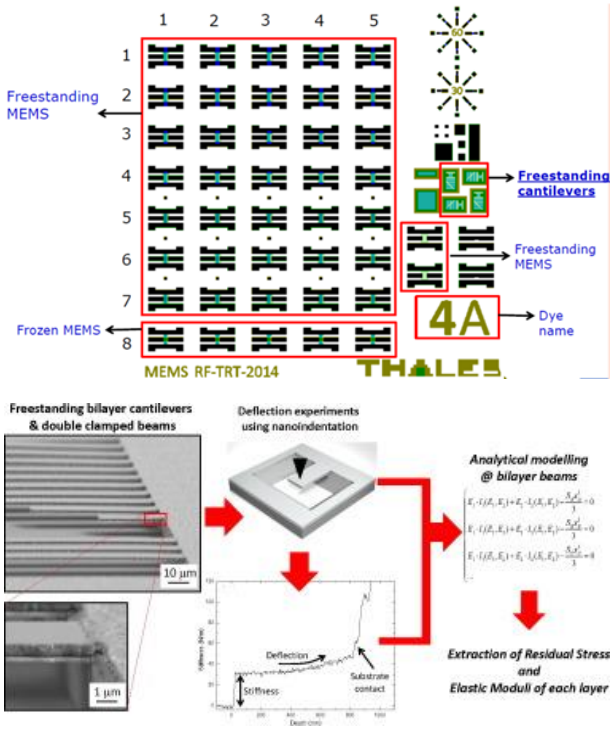

Fig. 32: Bilayer structure (TiW/Au) fabricated with photolithography mask (top) and specially developed nanoindentation method at Rome Tre to extract the elastic modulus

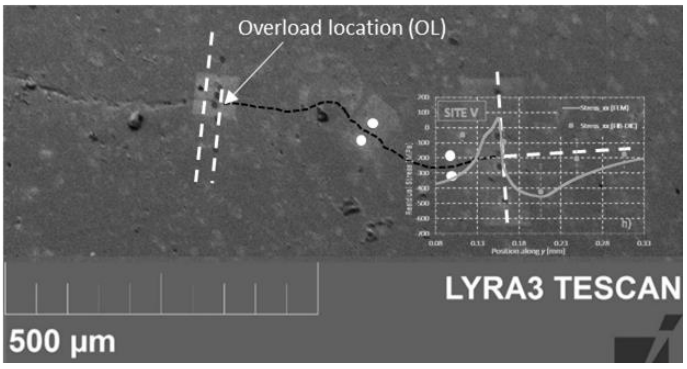

Fig. 33: Residual Stress measurements at the crack tip

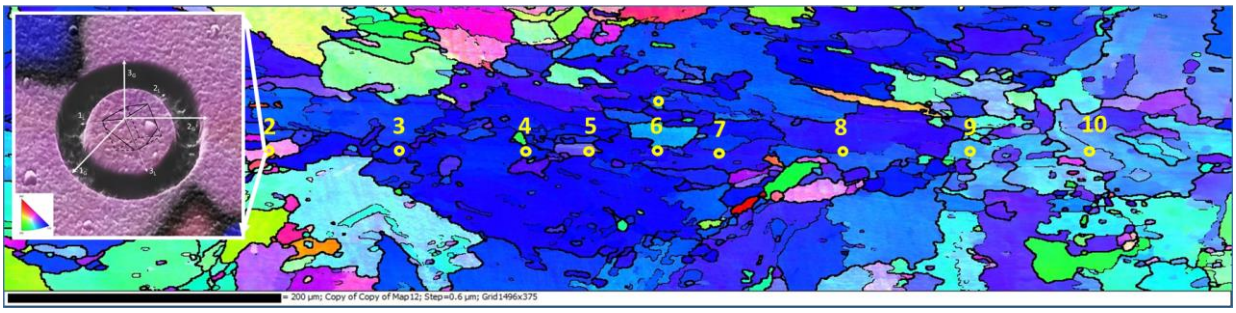

Fig. 34: Example of FIB-DIC residual stress measurement in a polycrystalline material

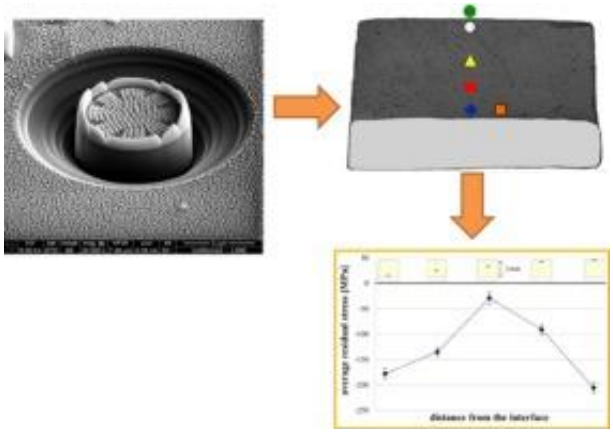

Fig. 35: Residual stress analysis in heat-pressed ceramic on zirconia core

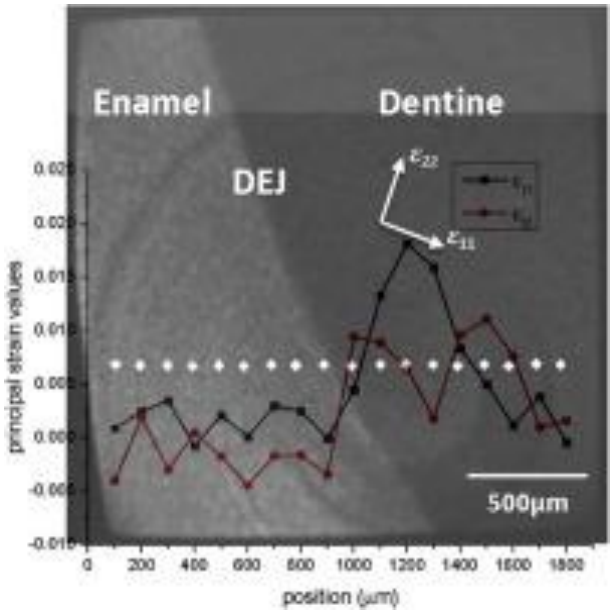

Fig. 36: Residual strain in human dentine and enamel

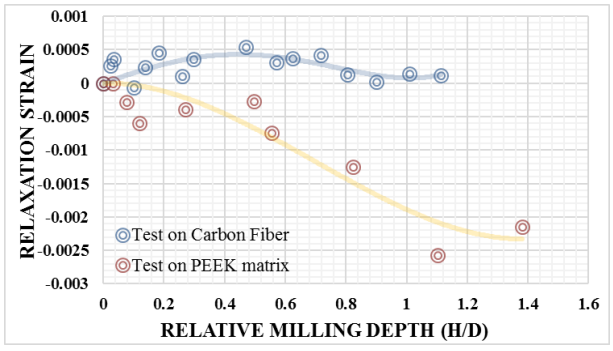

Fig. 37: Residual strain in carbon fiber and PEEK matrix

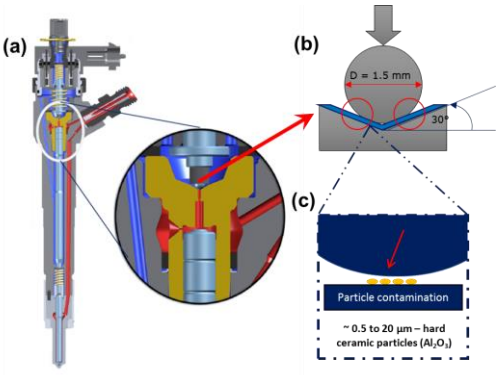

Figure 38 (a) A typical diesel injection system, (b) Ball valve design and (c) magnified view of the particle entrainment in the narrow gap between ball valve and counter body

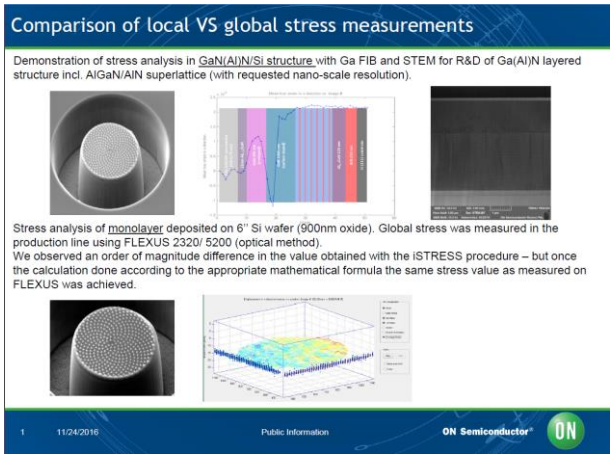

Figure 39 Upscaling of the FIB-DIC methodology at TESCAN